

# DESIGN ENHANCEMENT OF BIOMEDICAL SCAFFOLDS MADE BY SELECTIVE LASER MELTING

M. Speirs\*, G. Pyka†, J.-P. Kruth\*, J. Luyten†, J. Schrooten†, M. Wevers† and J. Van Humbeeck†

\* University of Leuven (KU Leuven), Department of Mechanical Engineering, Celestijnenlaan 300B, 3001 Leuven, Belgium

† University of Leuven (KU Leuven), Department of Materials Engineering, Kasteelpark Arenberg 44, 3001 Leuven, Belgium

## Abstract

Selective laser melting (SLM) is increasingly used to fabricate biomedical scaffolds. However, the intrinsic specifications of the process such as laser spot size, layer thickness, and particle size limit the production accuracy, altering the geometrical characteristics and mechanical properties of the scaffolds. This work attempts to assess and improve the mechanical properties of TiAl6V4 biomedical scaffolds by eliminating/modifying the sharp and thin nodes (as the main source of stress concentrations and lowering the mechanical properties). This is carried out through a gradual increase of the beam (strut) thickness around the nodes where corresponding struts meet. The compression performance of these scaffolds was assessed and compared to common examples (unaltered struts) and to scaffolds designed with thicker struts in the centre of the beams (demonstrating the largest contrast). The findings prove that the thickening of the nodal points improves the strain distribution while maintains the mechanical properties at an identical solid volume fraction. This can be used to improve the scaffold design by a gradual strut thickness (in a comparable volume fraction) for an improved bio-mechanical performance.

## 1. Introduction

Selective laser melting (SLM) is an additive manufacturing (AM) technique which fabricates three dimensional parts layer by layer from a defined CAD model. Thin layers of powder are melted upon one another locally with a laser beam. The process is repeated for subsequent layers until completion [1]. The layer-wise nature of the process allows production of complex customised parts such as biomedical scaffolds. An overview of the process is shown in figure 1.

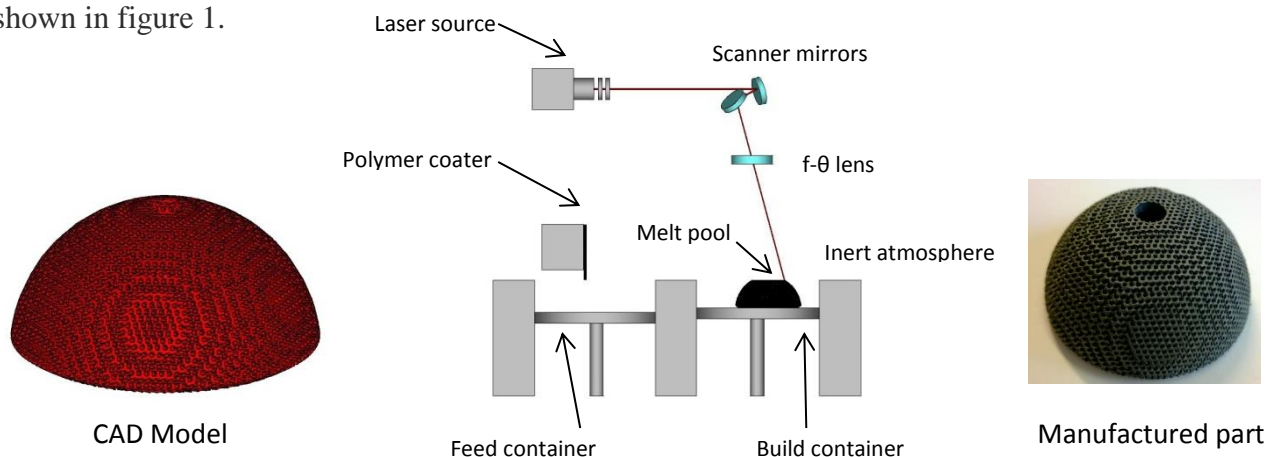


## Figure 1. Schematic illustration of the selective laser melting process (SLM).

Scaffolds are porous materials which assist in the healing of large bone defects. The use of scaffolds is to allow cell seeding and eventual vascularization of the implant while providing load bearing support. The mechanical properties are dependent on the material and on the geometrical features of the scaffold [2,3]. For bioresorbable and organic scaffolds the main focus is maximum surface area allowing minimal implant integration time with the implants volume fraction a minor consideration. For permanent metallic scaffolds there is no option for removal. Therefore, generating an implant with sufficient open porosity and minimal solid volume fractions and adequate mechanical properties is the key factor. Ti6Al4V is a common bio-compatible material with wide usage (enabling the comparison of the findings with other work).

So far, most work has focussed solely on production of uniform scaffolds with constant strut thickness and analysing methods of those products [4]. However, no attempt has been made to implement any gradual changes into the scaffold design in order to reinforce nodal zones against rupture/failure for load bearing applications. This study aims to assess the failure modes seen in scaffold production and to improve the mechanical properties (at a specific solid volume fraction) through reinforcing the selected zones of the scaffolds. A diamond unit cell is used with two variants. One is designed with enlarged nodal joints, in contrast to the one with increased thickness within the centre of the strut. They were designed at comparable overall solid volume fractions with three different strut sizes chosen for each design. These designs were also selected to allow comparison with previous work [2].

## 2. Materials and methods

### 2.1 Design and production

Selective laser melting was used for manufacturing porous titanium (Ti6Al4V-ELI) scaffolds using a diamond unit cell with two variations. One variation introduced a gradual increase in strut thickness from the centre of the beam to the node at a ratio of 2:1. The other variation incorporated the opposite with a gradually increasing thickness from the node to the centre of the beam at a ratio of 2:1. These two designs will be referred to as centrally thickened beam (CTB) and reinforced nodes (RN) along with the conventional diamond unit cell with constant strut thickness (Di): figure 2. Each design was created using Magics software [Materialise NV, Haasrode, Belgium].

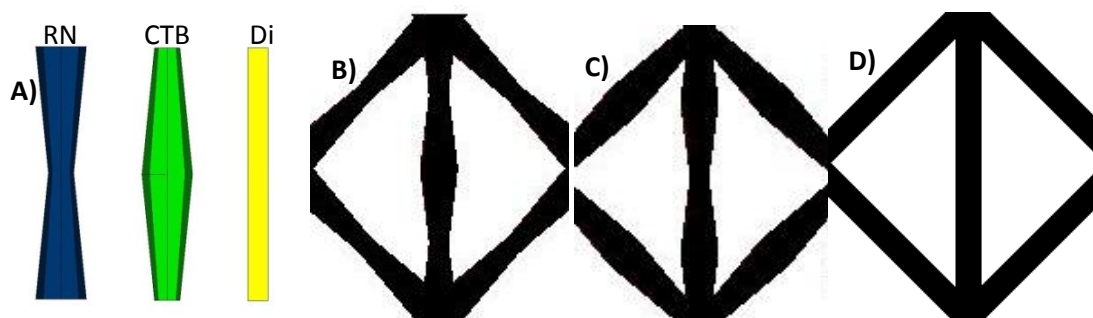


**Figure 2. CAD images of each beam for each design and the pore and strut size for one unit cell: A) different beam types (left to right as RN, CTB, Diamond), B) reinforced node (RN), C) centrally thickened beam (CTB) design, and D) conventional diamond**

All scaffold samples were designed with a height of 6.4mm and 6mm diameter with a constant pore size of 1000 $\mu$ m and varying strut sizes as shown in table 1. All samples were removed from the SLM base plate by EDM and then ground to a height of 6mm.

**Table 1. Overview of scaffold designs produced**

Scaffold Design	Strut diameter ( $\mu$ m)	Surface area ( $\text{mm}^2$ )	Volume ( $\text{mm}^3$ )	Designed Volume fraction (%)
Diamond	140	363	13.0	7.7
	160	401	16.4	9.7
	180	430	19.7	11.6
	200	459	23.4	13.8
Centrally Thickened Beam	100-200	338	12.2	7.2
	120-240	377	16.4	9.7
	140-280	443	22.3	13.2
Reinforced Nodes	100-200	310	10.9	6.4
	120-240	352	15.0	8.8
	140-280	423	21.4	12.6

The designed scaffolds were produced on an in-house developed SLM machine using an IPG Yb:YAG fibre laser of 300W with Ti6Al4V powder. All designs were produced with a 45 $\mu$ m beam offset Table 2 gives an overview of the powder specifications and SLM process parameters.

**Table 2. Specifications of the Ti6Al4V powder, produced bulk material, and SLM process parameters**

Specifications of the Ti6Al4V powder		SLM process parameters	
Density:	4.43g/cm <sup>3</sup>	Laser power:	42W
Average grain size:	10-45 $\mu$ m	Scanning speed:	260mm/s
E-modulus:	110GPa	Hatch spacing:	74 $\mu$ m
Tensile Strength (bulk material):	1000MPa	Layer thickness:	30 $\mu$ m
Yield stress at 0.2% deformation:	920MPa	Beam offset	45 $\mu$ m
		Beam diameter $\Phi_{1/e^2}$	52 $\mu$ m

## 2.2 Morphological Characterization

Microfocus X-ray computed tomography ( $\mu$ CT)-based morphological characterization of the Ti6Al4V scaffolds was performed using a Phoenix NanoTom S (GE Measurement and Control Solutions, Wunstorf, Germany) with a 180kV / 15 W high performance nanofocus X-ray tube and a 2304x2304 pixel Hamamatsu detector. A voltage of 90 kV and 240  $\mu$ A were applied. A tungsten target was used and a 0.3mm copper filter was installed. Each sample was scanned over 360 $^\circ$  with a 0.15 $^\circ$  rotation step, an exposure time of 500ms with no image skip

and no frame averaging was applied. After scanning reconstruction was completed using Phoenix datos/x 2.0 reconstruction software (GE Measurement and Control Solutions, Wunstorf, Germany). The resulting images had an isotropic voxel size of 6.5  $\mu\text{m}$ . CTAn software (Bruker micro-CT, Kontich, Belgium) was applied for 3D morphological analysis of the  $\mu\text{CT}$  data. Automatic Otsu segmentation [5] was applied for binarization of the reconstructed  $\mu\text{CT}$  images. For each geometry 3 samples were scanned. Additionally, an experimental strain analysis of one CTB and one RN sample was performed based on the non-rigid image registration of the  $\mu\text{CT}$  images [6-7]

Each type of scaffold was viewed using scanning electron microscopy (SEM; Phillips, XL 30, Germany) operating at 10kV. An ultrasonic cleaning in ethanol solution for 10 minutes was completed before analysis. The volume fraction and beam thickness were calculated for each design with the structure thickness calculated in 3D using a sphere fitting algorithm [8].

### **2.3 Mechanical characterization**

For mechanical testing, three as-produced samples of each design were compressed using an in house developed in-situ loading stage with maximum available load 30kN. A pre loading step of 0.01kN and a compression rate of 0.2mm/min was applied. The structural stiffness and ultimate compressive stress were calculated from the stress strain curves obtained from the load displacement data.

For strain mapping a radio-translucent micro-mechanical compression setup is used to apply and maintain strain for high resolution  $\mu\text{CT}$  scanning. To evaluate the local strain changes in function of displacement a constant compression rate of 0.2mm/min was applied followed by  $\mu\text{CT}$  scanning. A pre-load of 0.01kN was applied and then the reference scan of the non-compressed sample was applied. The sample was then compressed to 50% ultimate compressive strain (50% UCS) followed by  $\mu\text{CT}$  scanning. Both  $\mu\text{CT}$  images taken for each sample were registered to each other non-rigidly using Elastix software [8]. One CTB-140 and RN-140 sample were used for strain mapping due to their similar volume fractions post production.

## **3. Results and Discussion**

### **3.1 Morphological and Mechanical Characterization**

Despite the SLM potential to produce biomedical scaffolds, the geometry of the scaffolds is still restricted by the SLM characteristics such as laser spot size and layer thickness in table 2. Some of these issues are shown in figure 3. For example, struts of 100 $\mu\text{m}$  (designed strut thickness at the centre of the strut in figure 3B) are difficult to be achieved when a laser spot size of 80 $\mu\text{m}$  is used while the variation of beam diameter between layers is 10 $\mu\text{m}$ . On the other hand, even a thin layer thickness of 30 $\mu\text{m}$  has led to a pronounced staircase effect on the thin struts. The residual particles attached on the scaffolds (originating from the laser energy in margins of the spot diameter) are also evident. This is even more critical at nodes where the struts meet. The residual particles potential release post

implantation are an issue for the application (surface cleaning by chemical/electrochemical methods are usually followed to resolve this issue) [9].

In terms of design, the gradual increase of the strut was less pronounced compared to the CAD design file, once again due to working close to the machine limits, i.e., a laser spot size of 80 $\mu$ m used to melt thin struts (figure 3). This is even more evident for the RN scaffolds where the struts lowest diameter should be located in the centre of each strut (figure 3B).

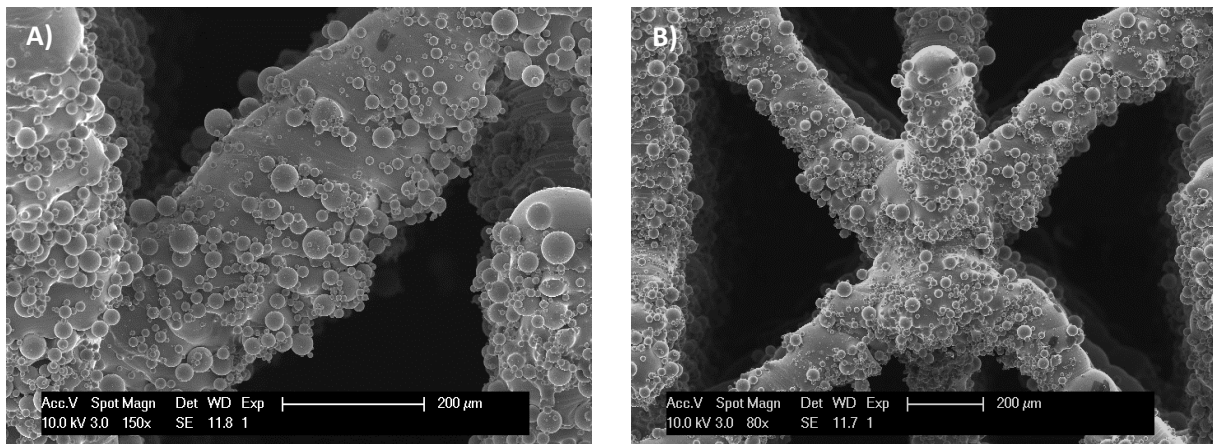


**Figure 3. SEM images of produced scaffolds: A) Centrally thickened beam (CTB) and B) Reinforced nodes (RN)**

### 3.2 Mechanical properties and Micro-CT analysis

The morphological parameters were assessed by micro-CT. The solid volume fraction was assessed and compared to the structural stiffness as shown in figure 4 for all produced designs. The average value for the 3 samples scanned and compressed is given. From the mechanical properties it can be seen that CTB showed a much lower stiffness at similar solid volume fractions when compared to the other two designs. It appears that RN performed equally with diamond.

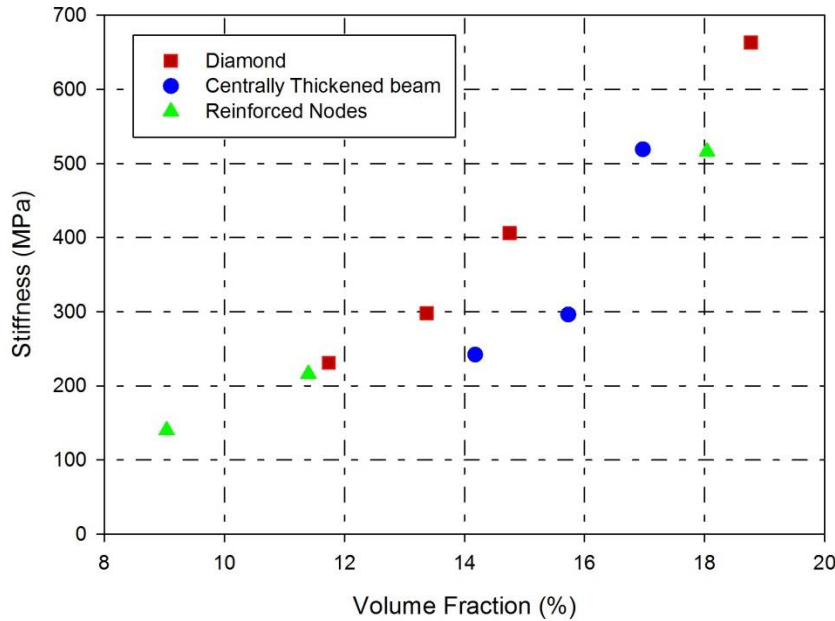


**Figure 4. Comparison of solid volume fraction in relation to stiffness for each design**

These issues result in analytical methods for unit cells producing theoretical stiffness much higher than those observed when using constant strut thickness in other studies [10]. A relationship between the Young's modulus and volume fraction scales on the power law and can be defined as:

$$\frac{E^*}{E_s} = C_1 \left( \frac{P^*}{P_s} \right)^2$$

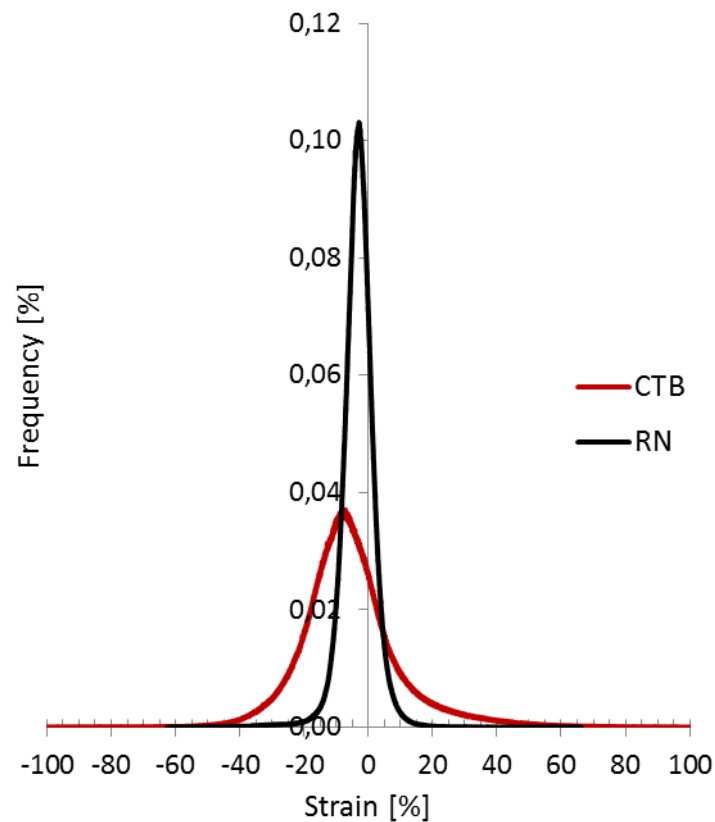
Where  $E^*$  = Youngs modulus of the scaffold,  $E_s$  = Youngs modulus of bulk materials,  $P^*$  = scaffold density,  $P_s$  = bulk density,  $C_1$  = constant dependent on cell geometry [11]. Where  $C_1 \leq 1$  and from analytical methods values of 0.98 are observed and from SLM produced Ti6Al4V  $C_1$  values of 0.1-0.3 are found in literature [2,4].

### 3.3 Local Strain Mapping

Figure 5 depicts a histogram of the volumetric strain calculated experimentally for CTB-140 and RN-140. As seen, the strain analysis revealed a large variation of strain frequency dependent on the design. The strain histograms of the RN-140 structure had a different bell-shape and asymmetry with respect to the mean value in comparison to CTB-140. In general, strain histogram analysis indicated a more homogenous strain distribution observed for RN-140 with high frequency of low compressive strains while CTB-140 revealed a wide range of compressive and tensile strains.

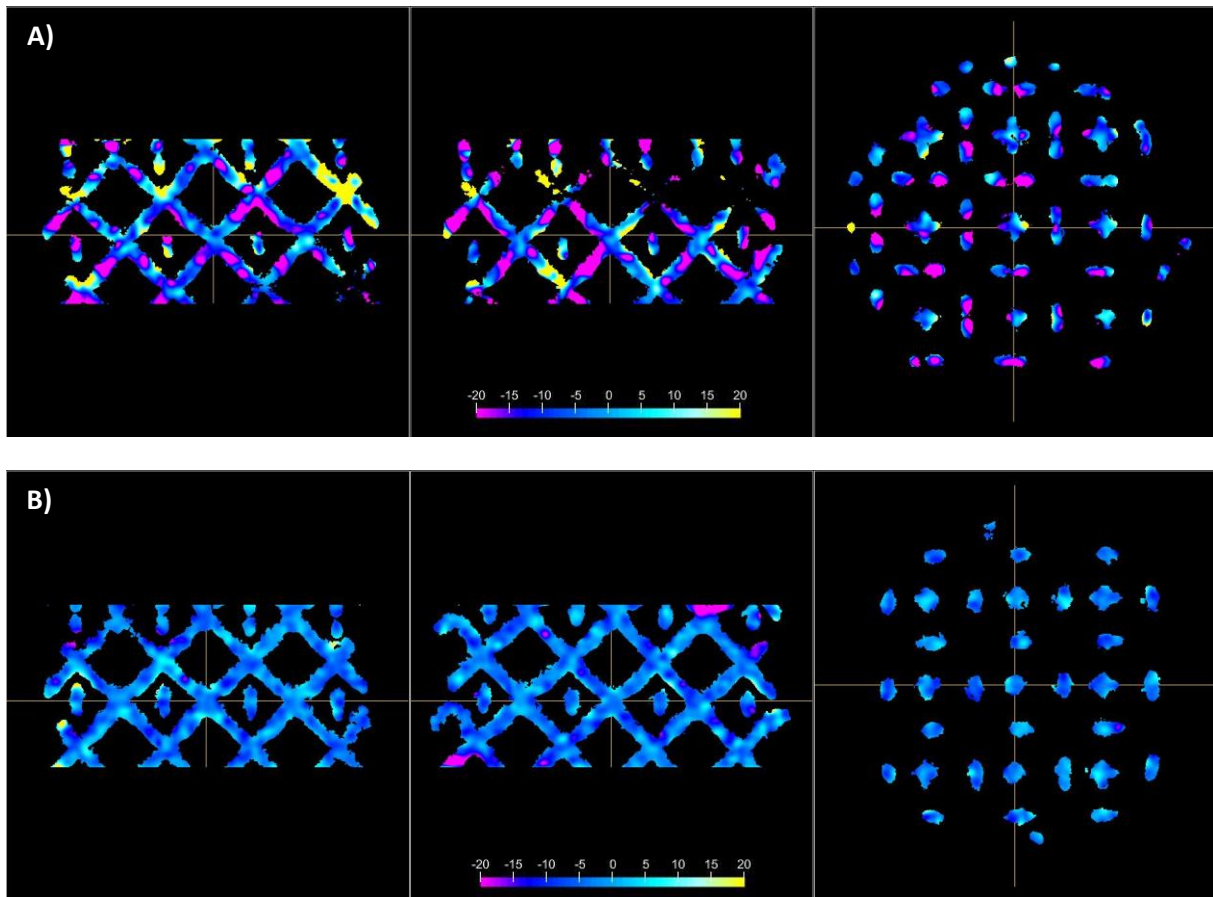
Analysis of the mean strain indicated differences in the level of the local deformations of the CTB-140 in comparison with RN-140 (4.3% and 5.9% of compressive strain for RN-140 and

CTB-140 respectively). Measurements of the most frequent (dominant) strain revealed a similar pattern (7.2% and 3.0% of compressive strain for RN-140 and CTB-140 respectively).



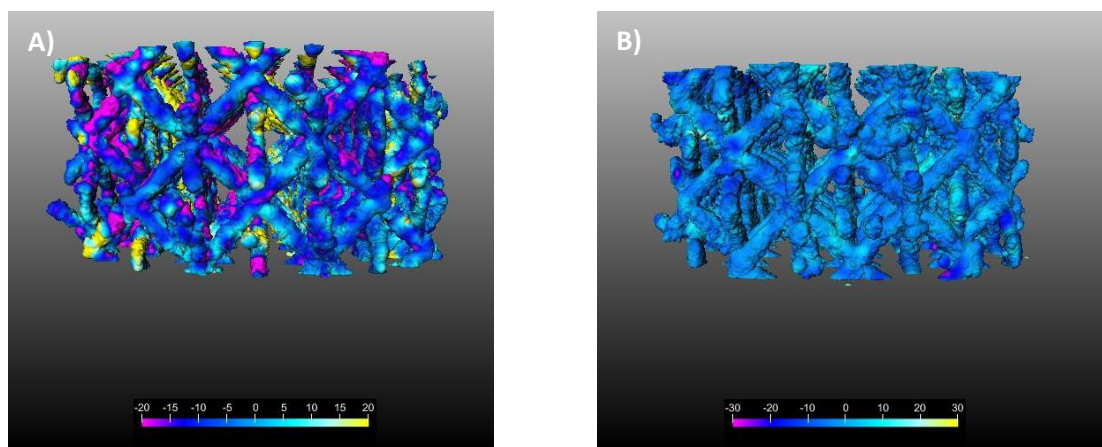
**Figure 5. Frequency of local distribution strain for CTB and RN at 50% of ultimate compressive strain (50% UCS)**

Figure 6 represents the 2D visualization of the strain computed for CTB-140 and RN-140 in the coronal sagittal and transverse slices. It can be shown that a more uniform strain is observed for RN-140. (Figure 6B). This confirms visually the differences in the strain histograms (Figure 5). CTB -140 shows large sections with high compressive strain (indicated in pink colour in Figure 6a). For RN-140 the largest compressive strains are observed at the centre of the beams. This is in contrast to CTB-140 where high compressive deformations were observed mainly in the connection between beams and nodes. Perhaps, thicker size of struts at central zones have led to a localized strain by further thickening of those areas in comparison with nodal joints where the struts have bended over and produced a tensile strain. In contrast, the gradual increase in strut thickness from the centre of the beam eliminated the amount of the critical points of the scaffolds. . Additionally, RN-140 revealed a more homogenous strain distribution across the scaffold structure in comparison to CTB-140 (Figure 6) which could be advantageous during implant loading triggering osteoinduction uniformly throughout the scaffold.



**Figure 6. Typical strain maps (coronal, sagittal and transverse) of the obtained 3D  $\mu$ CT images of the compressed Ti6Al4V scaffold designs showing the volumetric strain A) Centrally thickened beams (CTB) and B) Reinforced nodes (RN)**

In figure 7 a 3D visualization of the strain maps for CTB-140 and RN-140 are given, confirming the results present in two dimensions in figure 6. Once again, it can be observed that a large inhomogeneous deformation distribution of the CTB occurs in contrast with the very homogenous distribution of the deformation within the RN design.



**Figure 7. A 3D visualization of the local strain at 50% ultimate compressive strength for A) centrally thickened beam (CTB) and B) reinforced nodes (RN).**

As mentioned, the gradual change of strut thickness changed the scaffold architecture (figure 3), though it was restricted by the machine limitations (e.g. high comparative size of the laser beam diameter to the strut). The RN scaffolds showed a similar stiffness to the conventional diamond design, which was higher than CTB scaffolds. A more homogeneous deformation distribution was observed for the scaffolds designed thicker at the nodes leading to failure occurring at both nodes and struts. Higher deviation in the gradual designs should be followed in future works to better clarify the alternations in mechanical performance at similar volume fractions. Applying surface modification techniques (such as chemical/electrochemical etching) to remove the attached particles on these enhanced scaffolds is another promising aspect, pursued for future work.

#### **4. Conclusion**

This study assessed the strain distribution and structural stiffness for two variations of a standard diamond unit cell. For centrally thickened beam scaffolds (CTB) a lower stiffness was observed at similar solid volume fractions along with a largely inhomogeneous strain distribution. This was due to a larger amount of critical points throughout the scaffolds structure with elevated local deformation observed by local strain mapping experiments located mainly at the beam-node connections. For scaffolds with reinforced nodes (RN), the apparent compressive stiffness was equal to that of the conventional diamond at a similar volume fraction. Moreover, the reinforced nodes led to a very homogenous distribution of strains, being a promising aspect of the design.

For future work RN scaffolds could be used in conjunction with surface modification techniques used to remove residual grains after production [12]. This will allow compensation for material removal at the nodes resulting in more inhomogeneous strain distributions similar to those observed in CTB scaffolds.

#### **Acknowledgements**

The authors acknowledge support within the EU 7th framework programme FP7/2007-13 under Marie-Curie project grant No. 264635 (BioTiNet-ITN) and the Hercules foundation for founding the project AKUL/09/001 “Micro- and nano-CT for the hierarchical analysis of materials” and the IAP project P7/21 INTEMATE, “Multiscale mechanics of INTERface dominated MATERials”, for financial support.

#### **References**

- [1] J.-P. Kruth, G. Levy, F. Klocke, T.H.C. Childs, “Consolidation phenomena in laser and powder-bed based layered manufacturing,” *CIRP Annals - Manufacturing Technology*, Volume 56, Issue 2, Pages 730-759, 2007.
- [2] S. Van Bael, Y.C. Chai, S. Truscello, M. Moesen, G. Kerckhofs, H. Van Oosterwyck, J.-P. Kruth, J. Schrooten, 2012. “The effect of pore geometry on the in vitro biological behavior

of human periosteum-derived cells seeded on selective laser-melted Ti6Al4V bone scaffolds,” *Acta Biomaterialia*, Volume 8, Issue 7, Pages 2824-2834.

[3] S.M. Ahmadi, G. Campoli, S. Amin Yavari, B. Sajadi, R. Wauthle, J. Schrooten, H. Weinans, A.A. Zadpoor, “Mechanical behavior of regular open-cell porous biomaterials made of diamond lattice unit cells,” *Journal of the Mechanical Behavior of Biomedical Materials*, Volume 34, June 2014, Pages 106-115.

[4] G. Campoli, M.S. Borleffs, S. Amin Yavari, R. Wauthle, H. Weinans, A.A. Zadpoor, “Mechanical properties of open-cell metallic biomaterials manufactured using additive manufacturing,” *Materials & Design*, Volume 49, August 2013, Pages 957-965, ISSN 0261-3069.

[5] N. Otsu, “Threshold selection method from Gray-level histograms,” *Ieee transactions on systems man and cybernetics*, 1979. 9(1): p. 62-66.

[6] S. Klein, M. Staring, K. Murphy, M.A Viergeever, and J.P P, Elastix; a toolbox for intensity based medical image registration. *IEEE Trans Med Imaging*, 2010. 20(1): p. 196-205.

[7] Pyka, G., Van de Castele, E., Depypere, M., Kerckhofs, G., Schrooten, J., Maes, F., and Wevers, M. Evaluation of credibility and limitations of the non-rigid registration of micro-CT images as a tool for local strain analysis. *Bruker microCT User Meeting*. Ostend, Belgium, 5-8 May 2014.

[8] M. Bruker, CTAn UserManual [http://www.skyscan.be/next/CTAn\\_UserManual.pdf](http://www.skyscan.be/next/CTAn_UserManual.pdf). 2013

[9] G. Pyka, G. Kerckhofs, I. Papantoniou, M. Speirs, J. Schrooten, M. Wevers, 2013 “Surface roughness and morphology customization of additive manufactured open porous Ti6Al4V structures,” *Materials*, 6, 4737-4757.

[10] H. X. Zhu, J. F. Knott, N. J. Mills, “Analysis of the elastic properties of open-cell foams with tetrakaidecahedral cells,” *Journal of Mechanics of Physics and Solids*, Volume 45, 1997, Pages 319-343.

[11] L. Gibson, M.F. Ashby, B.A Harley “Cellular materials in nature and medicine,” Cambridge university press, Cambridge, 2010: Pages 31-44.

[12] G.Pyka, A.Burakowski, G. Kerckhofs, M. Moesen, S. Van Bael, J. Schrooten and M. Wevers, 2012. “Surface modification of Ti6Al4V open porous structures produced by additive manufacturing” *Advanced Engineering Materials*, 14, 363-370.